A Wearable Real-Time System for Simultaneous Wireless Power and Data Transmission to Cortical Visual Prosthesis

Gian Luca Barbruni, *Graduate Student Member, IEEE,* Francesca Rodino, *Graduate Student Member, IEEE,* Paolo Motto Ros, *Member, IEEE,* Danilo Demarchi, *Senior Member, IEEE,* Diego Ghezzi, *Senior Member, IEEE,* and Sandro Carrara, *Fellow, IEEE*

***Abstract*—Wireless, miniaturised and distributed neural interfaces are emerging neurotechnologies. Although extensive research efforts contribute to their technological advancement, the need for real-time systems enabling simultaneous wireless information and power transfer toward distributed neural implants remains crucial. Here we present a complete wearable system including a software for real-time image capturing, processing and digital data transfer; an hardware for high radiofrequency generation and modulation via amplitude shift keying; and a 3-coil inductive link adapt to operate with multiple miniaturised receivers. The system operates in real-time with a maximum frame rate of 20 Hz, reconstructing each frame with a matrix of 32 $\times$ 32 pixels. The device generates a carrier frequency of 433.92 MHz. It transmits the highest power of 32 dBm with a data rate of 6 Mbps and a variable modulation index as low as 8%, thus potentially enabling wireless communication with 1024 miniaturised and distributed intracortical microstimulators. The system is primarily conceived as an external wearable device for distributed cortical visual prosthesis covering a visual field of 20°. At the same time, it is modular and versatile, being suitable for multiple applications requiring simultaneous wireless information and power transfer to large-scale neural interfaces.**

***Index Terms*—Inductive Power Transfer; RF Transmitter; ASK Modulator; SWIPT; Implantable Medical Device; Distributed Neurostimualtors; Cortical Visual Prostheses.**

Manuscript received Month X, 2023; revised Month X, 2023; accepted Month X, 2023. Date of publication Month X, 2023; date of current version Month X, 2023.

Corresponding author: Gian Luca Barbruni.

Gian Luca Barbruni is with Bio/CMOS Interfaces Laboratory (BCI), École Polytechnique Fédérale de Lausanne, 2000 Neuchâtel, Switzerland and was also with Medtronic Chair in Neuroengineering, École Polytechnique Fédérale de Lausanne, 1202 Geneva, Switzerland. (e-mail: gianluca.barbruni@epfl.ch)

Francesca Rodino is with Bio/CMOS Interfaces Laboratory (BCI), École Polytechnique Fédérale de Lausanne, 2000 Neuchâtel, Switzerland. (e-mail: francesca.rodino@epfl.ch)

Paolo Motto Ros and Danilo Demarchi are with Department of Electronics and Telecommunications (DET), Politecnico di Torino, Turin, Italy. (e-mail: paolo.mottoros@polito.it; danilo.demarchi@polito.it)

Diego Ghezzi was with Medtronic Chair in Neuroengineering, Center for Neuroprosthetics and Institute of Bioengineering, School of Engineering, École Polytechnique Fédérale de Lausanne, 1202 Geneva, Switzerland and is now with Ophthalmic and Neural Technologies Laboratory, Department of Ophthalmology, University of Lausanne, Hôpital ophtalmique Jules-Gonin, Fondation Asile des Aveugles, 1002 Lausanne, Switzerland (e-mail: diego.ghezzi@epfl.ch)

Sandro Carrara is with Bio/CMOS Interfaces Laboratory (BCI), École Polytechnique Fédérale de Lausanne, 2000 Neuchâtel, Switzerland. (e-mail: sandro.carrara@epfl.ch)

Color versions of one or more of the figures in this article are available online at https://ieeexplore.ieee.org.

Digital Object Identifier 10.1109/TBCAS.2023.XXXXXXX

I. Introduction

WIRELESS, miniaturised and distributed implantable Brain-Machine Interfaces (BMIs) are rapidly emerging as a versatile, scalable and efficient technologies for monitoring and/or treating neural diseases and mental disorders [1], [2]. With respect to traditional implantable BMIs, distributed and miniaturised neural interfaces increase the bio-mechanical compliance, reduce the implantation trauma and expand the area of coverage across a wider region of the brain [3]. Technically, this is achieved by dividing the system into numerous miniaturised devices, each functioning autonomously and wirelessly. Recent advancements in microtechnology and Wireless Power Transfer (WPT) have facilitated the significant miniaturization of implantable devices to millimeter (or even sub-millimeter) scales [4]. Notable examples are: neural dust [5], neurograins [6], [7], FF-WINeR [8], and ENGINI [9].

Wireless, miniaturised and distributed BMIs are precursors for the advancement in the field of Cortical Visual Prosthesis (CVP), for which thousands of stimulating sites are needed for restoring an useful artifical vision [10]. WPT enabled the progress from a few tens of channels of the first implants [11], [12] to several hundreds of the last few years [13], [14]. Exploiting the wireless and distributed BMIs, it is now possible to envision thousands of miniaturised neurostimulators [6] in a one-to-one correlation with each pixel of the visual field. The development of wireless, miniaturised and distributed BMIs for CVP require external systems combining: i) real-time image acquisition and processing [15], [16]; ii) carrier frequency generation and modulation (hardware) [17], [18] and iii) WPT systems toward multiple miniaturised and distributed receivers [4], [9].

On the image processing side, the real-time operation is often achieved using Field Programmable Gate Array (FPGA) [19], [20], exploiting their high flexibility and programmability at the hardware low-level with a strong focus on performance maximization. However, this usually means a significant inherent added design complexity since the early development stages. Therefore, from a practical system-level proof-of-concept design perspective (as in this case), a higher-level software-based approach is highly beneficial for the higher degree of flexibility in quickly exploring and testing a much broader range of solutions.

On the transmission side, an high data rate has been ob-

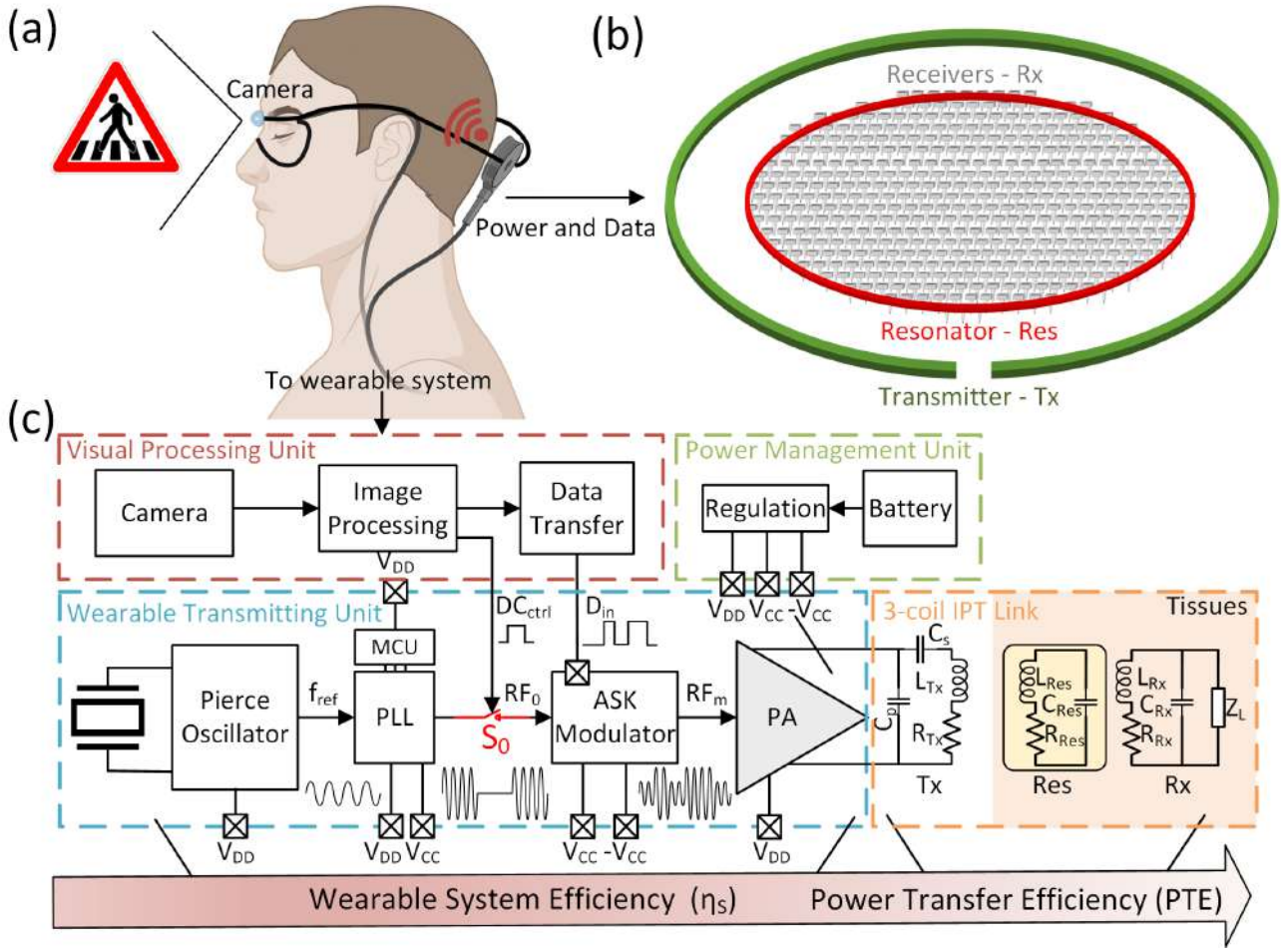

Figure 1. (a) General overview of a wireless and distributed cortical visual prosthesis. (b) Sketch of a 3-coil inductive link toward multiple miniaturised neural implants. (c) Block diagram of the real-time system for simultaneous wireless power and data transmission including the Visual Processing Unit (VPU, red), the Power Management Unit (PMU, green), the Wearable Transmitting Unit (WTU, blue) and the electrical equivalent model of the 3-coil IPT link (orange), including transmitter coil (Tx), resonator coil (Res) and receiver coil (Rx).

tained by sending power and data via Inductive Power Transfer (IPT) through different wireless channels (i.e., different coils) [21]. However, this would require two antennas at the implant side, being not suitable in the case of miniaturised and distributed implants. Therefore, different Simultaneous Wireless Information and Power Transfer (SWIPT) systems have been developed exploiting WPT via IPT [4] with various modulation techniques [17], such as On-Off Keying (OOK) [22] or Amplitude Shift Keying (ASK) [23]. However, notwithstanding its importance, limited research focused on combining real-time operations and SWIPT in a single compact system enabling powering and communication with thousands of miniaturised implants at the same time.

In this paper, we present a wearable real-time system for simultaneous wireless information and power transfer to distributed cortical visual prosthesis via 3-coil inductive link. The system considers most of the constraints of a CVP made up of thousands of miniaturised, distributed and individually-addressable neurostimulators, such as real-time operation, frame rate, single-band powering frequency, communication data rate, output power and Specific Adsorption Rate (SAR) [24], [25].

II. Materials and Methods

Figure 1(a) shows a general overview of a wireless and distributed cortical visual prosthesis. A pair of spectacles record the images which are processed in real-time through a wearable system which simultaneously transmits power and data via 3-coil IPT to the implants (Figure 1(b)). The wearable system architecture is shown in Figure 1(c) as a block diagram. It is constituted by the Visual Processing Unit (VPU), the Power Management Unit (PMU) and the Wearable Transmitting Unit (WTU). In particular, the VPU operates in real-time on the images extracting the relevant information to trigger the WTU. For each frame, the WTU generates the modulated RF carrier signal for SWIPT to the implants. The PMU includes a battery pack and the power converters to supply all the components (i.e., VPU and WTU). In this scenario, the entire wearable system is connected to both

the camera and the transmitting coil (Tx), which are fixed respectively on the front and on the back of the spectacles.

The VPU includes the camera (C270 HD, Logitech) with maximum resolution of 720×720 pixels, diagonal field of view of 55° and acquisition frame rate of 30 Hz, connected via USB to the image processing module (Raspberry Pi4 Model B) with CPU Quad-core Cortex-A72 (ARM v8), Raspbian OS and equipped with 4GB SDRAM. Digital DC_{ctrl} signal is generated by the I/O pins of the Raspberry (RPi) while the digital data D_{in} are sent at high speed by the USB-to-serial/FIFO development data transfer module (FT2232H, FTDI) via SPI protocol exploiting USB 2.0 Full Speed communication (i.e., theoretical maximum speed of 12 Mbps). The software is implemented in Python and runs automatically once the RPi is turned on. The algorithm starts by cropping the acquired image according to the maximum covered visual field of the CVP [10] (i.e., 20°). Then, RGB-images are converted into grey-scale using the weighted RGB to grayscale conversion, as in (1):

$$Gray = 0.2989R + 0.5870G + 0.1140B \tag{1}$$

Contrast is adjusted differently for indoor and outdoor recording. For indoor images, local contrast is enhanced using the contrast-limited adaptive histogram equalization technique to better highlight the contours of objects. For outdoor images, the grey-scale is redistributed towards higher values to reduce details and uniform brightness. A median filter is then applied to remove the salt and pepper noise preserving the contours of objects, which is fundamental for the subsequent edge detection. In particular, each pixel is filtered with a 5×5 median kernel. Segmentation is performed using edge detection technique. For each pixel, a Sobel method is implemented to calculate the horizontal and vertical gradient with two 3×3 kernels. Dilation is then performed with a 7×7 kernel to enlarge and uniform the edge detected with the Sobel method.

The WTU includes the quartz crystal (NX5032GA, NDK), the Phase-Locked Loop (PLL - LTC6948-1, Analog Devices), the MicroController Unit (MCU - MSP430G2553, Texas Instruments), the switches (M3SW-2-50DRA+, Minicircuits), and the Power Amplifier (PA - RF6886, Qorvo). The MCU is used to automatically program the PLL at the system start-up. In particular, the PLL registers are filled via SPI interface. The PMU includes a 5 V, 3 A rechargeable battery (B30224, EC Technology) used for V_{CC} and a series of DC/DC converters to supply all the system. In particular $-V_{CC}$ = -5 V and V_{DD} = 3.3 V are respectively generated with NMR100C, Murata and TSR3-0533, Traco Power.

The WTU circuit is designed in Altium Designer® and manufactured in 0.36 mm-thick Isola 400 FR4 substrate (i.e., dielectric constant D_k = 3.90 and dissipation factor D_f = 0.02). All the traces driving RF_0 and RF_m (Figure 1(c)) are designed according to the critical length L_c = 2 cm, calculated as $\lambda_g/16$ [26], where λ_g is the guide wavelength, as in (2):

$$\lambda_g = \frac{c}{f_c \cdot \sqrt{\epsilon_{eff}}} \tag{2}$$

where c is the speed of light, f_c is the operating frequency (i.e., $RF_0 = 433.92\ MHz$) and ϵ_{eff} is the effective dielectric constant of the substrate. Considering $\epsilon_{eff} = D_k$, microstrip lines longer than 2 cm with characteristic impedance Z_{line} are matched at Z_0 as in (3) [27]:

$$Z_{line} = \frac{87}{\sqrt{D_k + 1.41}} ln\left[\frac{5.98 \cdot T_s}{(0.8W + T)}\right] \tag{3}$$

where W and T are respectively the width and the thickness of the strip line and T_s is the substrate thickness. With the chosen thin substrate (T_s = 0.36 mm) and a standard copper trace thickness (i.e., T = 35.56 μm), the calculated and used strip line width is 0.71 mm at Z_0.

The entire system is packaged in a 3D-printed plastic case designed in Fusion 360 software from Autodesk®. The case cover is printed by multi-jet modeling technology in VeroClear (e.g., rigid and transparent resin). The case substrate is printed by selective laser sintering technology in polyamide-12 (i.e., higher flexibility for enhancing the opening of the case).

The PA output is connected with a short coaxial cable to the Tx which is fixed on the back of the spectacles and aligned with the resonator to the implants. The entire wearable system (from the camera to the Tx) operates starting from the rechargeable battery with a total wearable system efficiency η_S. Then, the electrical equivalent model of the 3-coil IPT link is highlighted in Figure 1(c) (orange box). The IPT link is optimised and simulated in Ansys HFSS®, evaluating the coils' characteristics and the Power Transfer Efficiency (PTE) following the Rx optimisation algorithm [25]. The Tx, modelled with inductance L_{Tx} and resistance R_{Tx}, is a circular single-turn copper coil with outer diameter of 25 mm, trace width of 5 mm and trace thickness of 35 μm. The copper trace is left uncovered (i.e., no soldermask layer) to increase the current density flux and, thus, the induced magnetic field. The Impedance Matching Network (IMN) includes C_s and C_p whose nominal values are respectively calculated from the series equivalent reactance and the parallel reactance of the network. In particular, C_s = 4.04 pF and C_p = 38.04 pF for L_{Tx} = 36.9 nH and R_{Tx} = 1.8 Ω perfectly matched at Z_0 = 50 Ω. The Tx with the IMN (Figure 1(c)) is simulated in LTSpice® and Ansys HFSS®, laid out in Altium Designer® and fabricated in a 1.55 mm-thick FR4 substrate. C_s and C_p are two trimmer capacitors (JR150 in the range 3-15 pF and JR500 in the range 8-50 pF respectively, Voltronics) accounting for environment and coupling variation during testing (i.e., air or ex-vivo).

The resonator coil (Res), modelled with inductance L_{Res} and resistance R_{Res}, is a single-turn circular copper coil with outer diameter of 14 mm, trace thickness of 25 μm and trace width of 0.1 mm encapsulated in a 300 μm polyimide and matched with the variable parallel capacitor C_{Res} (JR150, Voltronics) at 433.92 MHz. The receiver coil (Rx), modelled with inductance L_{Rx} and resistance R_{Rx}, is a miniaturised 4-turn wire wounded coil with an inner diameter of 200 μm and a circular-section insulated copper wire with diameter of 200 μm and pitch of 200 μm, matched with the variable parallel capacitor C_{Rx} (JR150, Voltronics) at 433.92 MHz. Each coil and the full IPT link are characterised both in air and in ex-vivo. In the ex-vivo setup, the Rx is placed above a 50 mm-thick beef while a 14 mm-thick beef is interposed

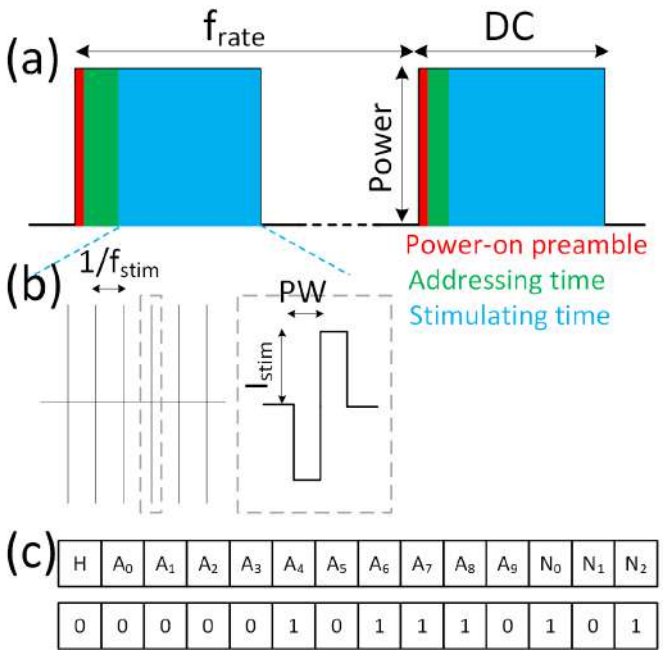

Figure 2. (a) Timely division for the duty-cycled transmission including the Power-on preamble (red) for implant rectification; the Addressing time (green) for data transmission; and the Stimulating Time (blue) where RF power is continuously delivered to the implants. (b) Graphical representation of the current-controlled stimulation waveform delivered by each called neurostimulator continuously powered via IPT. (c) General data transmission for the 14-bit string with a representative example including the fixed payload header H (0), 10 bits ($A_0 - A_9$) for the 1024 implants identification and 3 bits ($N_0 - N_2$) for stimulation programming.

among the Tx and the Rx (with and without the Res), similarly to [28], [29]. Characteristic coils' impedance, S_{11} and S_{21} measurements are conducted using Vector Network Analyzer (VNA) (ZVL, Rohde&Schwarz).

The VPU generated digital signals (i.e., DC_{ctrl}, D_{in}) are characterised and measured using a logic analyzer (Logic Pro 16, Saleae). The WTU generated analog signals (i.e., f_{res}, RF_0, RF_m) are measured using standard characterisation equipment (DSO-X 4104A, Keysight).

III. Results and Discussion

Globally, the system operates in a time-locked manner defined and triggered by the VPU (Figure 2(a)). An image is acquired by the external camera at specific frame rate f_{rate} (i.e., f_{rate} = 10 Hz). Each transmission includes: i) the power-on preamble (red) needed for the neural implant start-up (i.e., rectification); ii) the addressing time (green) where the digital information related to the recorded and processed image are transmitted by modulating the powering carrier signal and iii) the stimulating time (blue) in which power is continuously transmitted allowing each battery-less implant to deliver programmable electric pulses. The biphasic stimulation waveform is shown in Figure 2(b) where N pulses of amplitude I_{stim} and pulse width PW are delivered at the burst rate f_{stim}. Data are transmitted as serial and subsequent packets of 14-bits-strings as in Figure 2(c) (i.e., each string represents an active pixel on the recorded image). For each string, the first bit represents the header H fixed at the low logical state (0), 10 bits identify the active pixel (i.e., addressing each of the 1024 implants) and 3 bits program the neurostimulation pattern (i.e., N or f_{stim} or both). Overall, the system continuously delivers power via IPT for the entire duration of the transmission (power-on preamble + addressing time + stimulating time). The system should operate according to regulatory requirements. The most stringent parameter is the SAR for the human head, which overall limits the maximum power wirelessly delivered to the implants. The maximum averaged SAR is country-specific: in the USA it is fixed to 1.6 W/kg for 1 g of tissue mass measured during 30 min of exposure [4]. Being the SAR-constrained power delivered to the load usually limited for ultra-miniaturised receivers [24], the transmission must be duty cycled, as in [30]. In particular, the VPU triggers the duty cycle (DC) for each transmitted block (i.e., DC = 10%, Figure 2(a)). In other words, the system continuously delivers power via IPT at f_{rate} with a fixed DC according to the SAR limits.

A. Visual Processing Unit

The VPU is designed to operate in real-time on the frames acquired by the camera triggering both DC_{ctrl} and D_{in} operating on the WTU for the modulated and duty cycled wireless transmission.

Figure 3 shows the steps of the image processing algorithm considering a static image acquired by the camera (instead of a real-time video) and obtaining a final image with 32×32 pixels. In particular, the original frame (Figure 3(a)) is cropped into a squared gray-scale image covering a field of view of 20° (Figure 3(b)). Then, the outdoor image is adjusted in the contrast (Figure 3(c)), filtered with the median function (Figure 3(d)), segmented by means of edge detection through Sobel method (Figure 3(e)), dilated for contour definition (Figure 3(f)) and reconstructed with the chosen matrix of 32×32 pixels (Figure 3(g)) for a one-to-one correspondence with 1024 implants. The obtained processed image (Figure 3(g)) clearly defines the relevant details acquired by the original image, highlighting the contour of the pedestrian crossing. The 32×32 pixels output image represents a visual field with a coverage of 20°. Therefore, the entire field of view of the blind is reconstructed by consecutive scanning of the environment frame by frame at the operating frame rate.

At the end, for each frame every active pixel is converted into a binary string (Figure 2(c)) and sent by universal asynchronous receiver-transmitter communication to the FTDI chip for high-speed data transfer to the WTU (i.e., D_{in} transmitted at f_{data} = 6 Mbps). The chosen FTDI limits the maximum speed in communicating with the WTU. At the same time, a control signal DC_{crtl} triggers the WTU for duty cycling the wireless transmission (Figure 2(a)).

The start-up time of the VPU is 38.7 ± 1.7 s, mostly needed for the RPi to automatically turn on and launch the main code

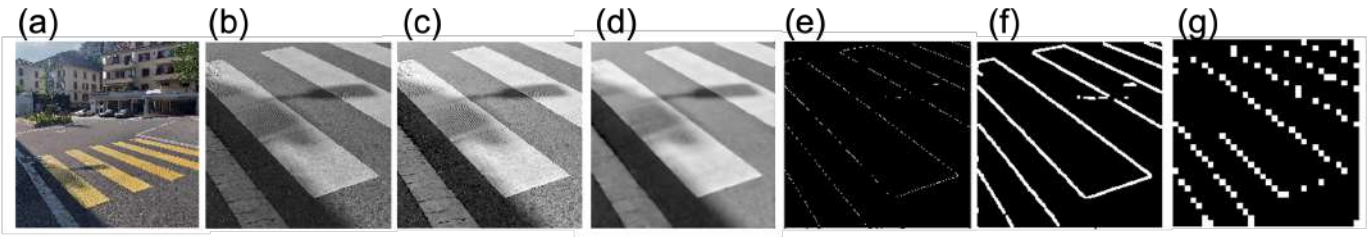

Figure 3. Steps of the image processing algorithm starting from (a) the original acquired RGB-image and proceeding with (b) cropping for a field of view of 20° and gray scale conversion; (c) outdoor contrast adjustment; (d) median filtering; (e) segmentation through Sobel method, (f) dilation and (g) reconstruction with a matrix of 32×32 pixels.

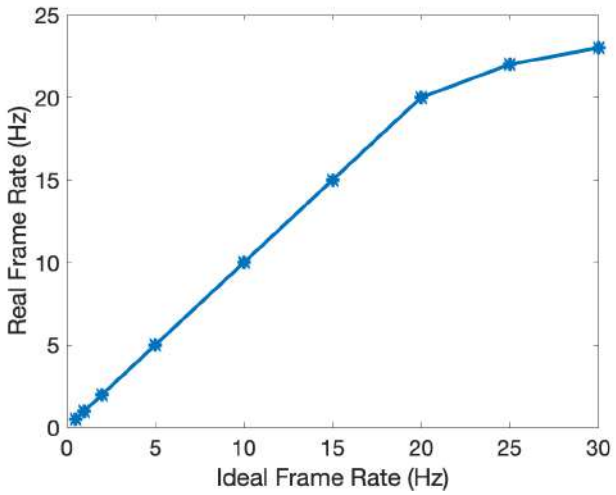

Figure 4. Real time frame rate performances of the VPU as a function of the ideal desired frame rate. The system operates in a linear fashion till 20 Hz.

for the continuous real-time operation. The system works in a linear fashion for frame rates lower than 20 Hz (Figure 4). The image processing computational time limits the maximum frame rate to 20 Hz. Being RPi a processor-based systems, the VPU performance has been tested to assess its stability among different frames. In particular, for a nominal VPU f_{rate} = 10 Hz the maximum variation among frames is in the range 9.98 - 10.02 Hz, meaning a 0.2% variation with the nominal frame rate, and, therefore, a stable real-time performance. Similar analysis has been performed for: i) the power-on preamble time for a nominal value of 450 μs leading to a variation of 4.4% among different frames and ii) the DC_{ctrl} time for a nominal value of 10 ms (i.e., DC = 10% for f_{rate} = 10 Hz) resulting in a variation of 0.04% among different frames. As expected, for times in the ms-range the VPU maintains a high performance level for real-time operations, which decreases as the required confidence level increases (i.e., higher variation for the power-on preamble time in the sub-ms range).

B. Wearable Transmitting Unit

The simplified WTU architecture is shown in the blue dashed box of Figure 1(b), which is a revised version of [31]. When powering miniaturised neural implants, the transmitted

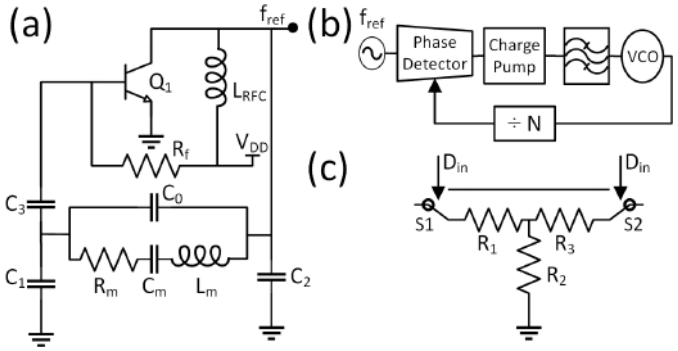

Figure 5. WTU main components: (a) Pierce oscillator, (b) PLL, (c) ASK-modulator.

carrier frequency should be higher than a few hundred of MHz to match the Rx lateral size and lower than a few GHz to limit the tissue losses [32]. Therefore, the Pierce Oscillator (PO) generates the reference frequency f_{ref} (i.e., 13.56 MHz) starting from a high-precision quartz crystal (i.e., described by the lumped model C_0, R_m, C_m and L_m in the schematic of Figure 5(a)). Then, the PLL is used to obtain the required carrier frequency RF_0 (i.e., 433.92 MHz) starting from f_{ref} through a feedback control system [31] (Figure 5(b)). In particular, f_{ref} is multiplied by N = 32 to obtain RF_0 (i.e., 433.92 MHz signal with a power of 1.5 dBm at Z_0) which is duty-cycled at DC through the switch S_0 triggered by DC_{ctrl} signal from the VPU. The ASK modulation is performed by two switches S_1 and S_2 symmetrically triggered at high speed through the D_{in} signal, which is generated in real-time by the VPU (Figure 5(c)). When S_1 and S_2 are turned on $RF_m = RF_0$ (i.e., high amplitude). When S_1 and S_2 turned off RF_m is attenuated by the T-pad structure, thus operating on the Modulation Index (MI). The modulator is a T-power-attenuator consisting of three resistors R_1, R_2 and R_3 (Figure 5(c)). Then, the class-AB PA drives the modulated high-power RF_m to the matched Tx [31].

Figure 6 shows two different MI emulating the ASK-modulated signal D_{in} with a 1 MHz squared digital waveform with a duty cycle of 50%. In particular, MI = 13.8% for R_2 = 120 Ω resulting in a maximum transmitted power of 32 dBm (2.55 V_{pp}) and 30 dBm (1.93 V_{pp}) respectively for the high and low amplitude levels (Figure 6(a) where RF_m has been attenuated by 20 dB for instrument protection). Then, MI =

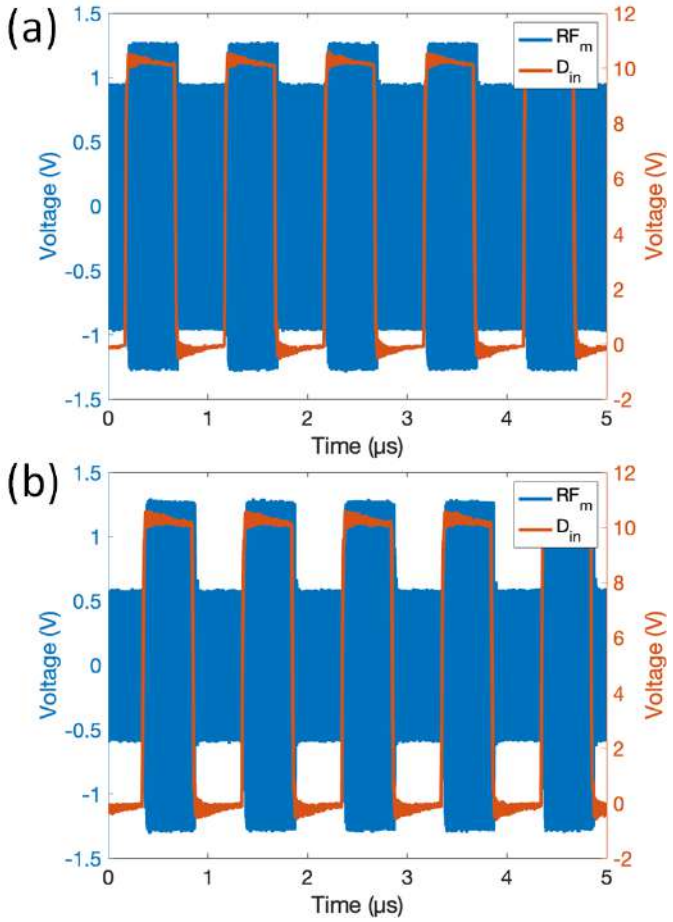

Figure 6. Modulation Index (MI) variation of the ASK-modulated RF_m using a 1 MHz squared digital waveform with a duty cycle of 50% as modulation D_{in}. (a) MI = 13.8% for R_2 = 120 Ω and (b) MI = 37% for R_2 = 60 Ω.

37% for R_2 = 60 Ω resulting in a maximum transmitted power of 32 dBm (2.55 V_{pp}) and 25.5 dBm (1.17 V_{pp}) respectively for the high and low amplitude levels (Figure 6(b) where RF_m has been attenuated by 20 dB for instrument protection). The WTU is modular and works for data rates as high as 20 Mbps and MI as low as 8% [31]. The latter is modified by tuning R_2 at the T-pad level of the ASK-modulation circuit (Figure 5(c)).

C. Inductive Link

Table I summarizes the measured characteristics of the coils constituting the 3-coil IPT link respectively in air and in ex-vivo (with tissues). As expected, the presence of tissues overall influences the quality factor (Q) of the coils and shifts their Self Resonance Frequency (SRF) toward lower frequencies. Therefore, all the matching networks are adjusted based on the experimental environment (air or ex-vivo) by tuning the variable capacitors. Figure 7(a) shows the ex-vivo experimental setup for the 3-coil IPT-link characterisation including Tx, Res and Rx. Figure 7(b),(c) respectively show the setup top view highlighting the Tx with its CC-IMN and the setup

Table I: SPECIFICATIONS OF THE 3-COIL IPT LINK.

	Parameter	Measurement	
		Air	Tissues
Tx	L (nH)	36.9	37.2
	R (Ω)	1.8	3.8
	Q at RF_0	55.9	26.7
	SRF (MHz)	893	843
	D_o (mm)	25	
	n	1	
	w (mm)	5	
	s (mm)	N/A	
	t (μm)	35	
Res	L (nH)	60	63.8
	R (Ω)	3.6	5.9
	Q at RF_0	45.4	29.5
	SRF (MHz)	1138	1085
	D_o (mm)	14.7	
	n	1	
	w (mm)	0.1	
	s (mm)	N/A	
	t (μm)	25	
Rx	L (nH)	11.5	11.6
	R (Ω)	0.55	0.58
	Q at RF_0	56.9	54.6
	SRF (MHz)	1661	1553
	D_o (μm)	600	
	n	4	
	w (μm)	200	
	s (μm)	N/A	
	p (μm)	200	

bottom view highlighting the Res and the miniaturised Rx. Figure 7(d) shows the simulated SAR constituting the 3-coil IPT link. The maximum SAR is 6.3 W/kg at muscle level for a 32 dBm transmitted power. Exploiting the developed 10% duty-cycled transmission [30], the maximum time-averaged SAR is reduced to 0.63 W/kg (i.e., three times lower than the maximum allowable SAR), ensuring a safe inductive link for powering 1024 miniaturised implants. Figure 7(e) compares the measured S_{21} with the 3-coil and the sub-optimal 2-coil IPT link respectively in air (red and black) and with tissues (blue and green). The PTE is calculated starting from the measured S_{21} [33] as in (4):

$$PTE_{\%} = \frac{|S_{21}|^2 R_L}{50\ \Omega} \cdot 100 \tag{4}$$

where S_{21} (in U) represents the ratio among the received power at the Rx with respect to the transmitted one from the Tx (14 mm away), and R_L is the load resistance (i.e., 50 Ω). The peak PTE is 0.72% with tissues at 433.9 MHz and increases to 4.3% in air at 440 MHz. It is worth to notice that being the IPT system optimised for the ex-vivo environment, a 7 MHz peak shift is highlighted when moving the setup in air. The result is highly consistent with previous IPT characterisation operating at lower frequency and relying on a similar setup [33]. The perfectly matched condition is achieved

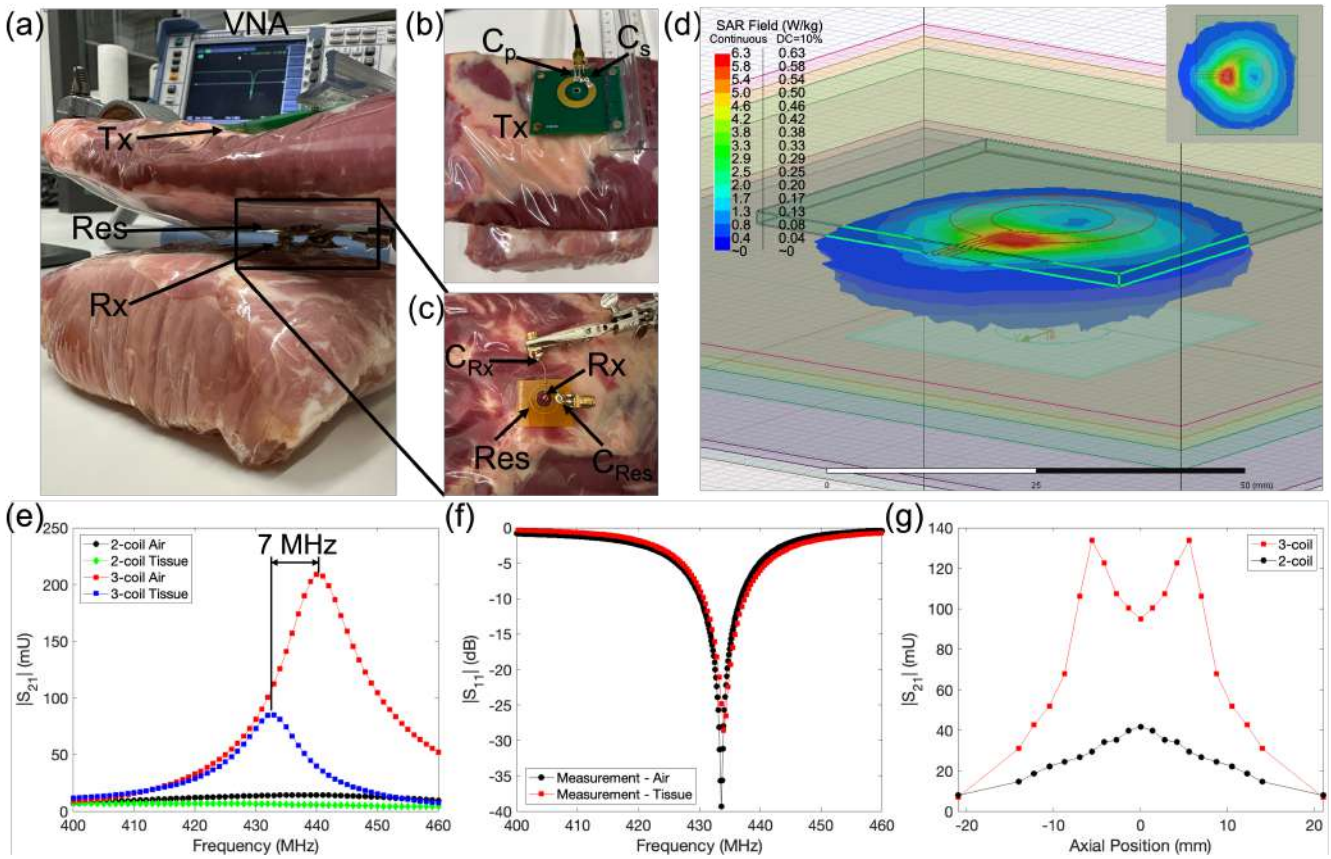

Figure 7. (a) Ex-vivo testing setup of the 3-coil IPT link including Tx, Res and Rx. (b) Top view of the setup highlighting the Tx and the CC-IMN and (c) bottom view of the setup highlighting the Res and the miniaturised Rx, respectively with their matching networks. (d) SAR simulation of the 3-coil IPT link. (e) Measurements of the S_{21} modulus for the 3-coil and 2-coil IPT link respectively in air (red and black) and with tissues (blue and green) highlighting a 7 MHz frequency shift when changing the setup from ex-vivo to air. (f) Measurements of the S_{11} modulus for a perfectly matched Tx in air (black) and in ex-vivo (red) after optimising the CC-IMN for the two environmental setups at Z_0. (g) Measurements of the S_{21} modulus for the optimised 3-coil IPT link (red) compared with the 2-coil IPT link (black) in air as a function of the Rx axial position with respect to the perfectly aligned and centered condition (i.e., 0 mm).

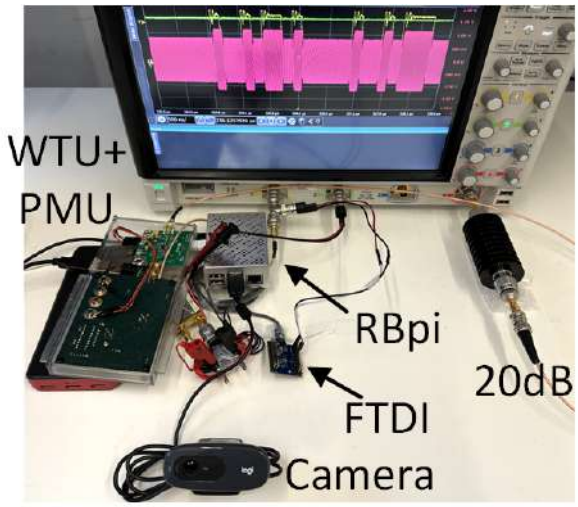

Figure 8. Testing setup of the real-time system adapted for the acquisition of the displayed signals (i.e., cables, connectors and attenuator).

by opportunely tuning the matching networks according to the experimental environment (air or tissues). Indeed, Figure 7(f) shows the measured S_{11} for the perfectly matched Tx operating in air (black) and in ex-vivo (red). Results highlight a 10.9 dB decrease in the reflection peak with tissues (peak of 28.4 dBm) compared to air environment (peak of 39.3 dBm). Figure 7(g) shows the modulus of the S_{21} (in mU) measured in air for the optimised 3-coil IPT link (red) and compared with the sub-optimal 2-coil IPT link (black), in which the resonator is not used. With a 3-coil IPT link, the large area underneath the resonator is covered showing the classical "M" shape with a maximum PTE of 1.77% and a minimum PTE at the center for a perfectly aligned Rx (i.e., 0.9% at 0 mm of relative axial position). On the contrary, for a 2-coil IPT link the maximum PTE drops to 0.17% for the Rx perfectly aligned with the center of the Tx (i.e., 0 mm of relative axial position) and progressively decreases with the Rx axial movement. Despite the 3-coil IPT link improvements, as expected, PTE remains limited for miniaturised Rx [24]. Transmitting 32 dBm via 3-coil IPT with a peak PTE of 0.72% at 433.92 MHz results in

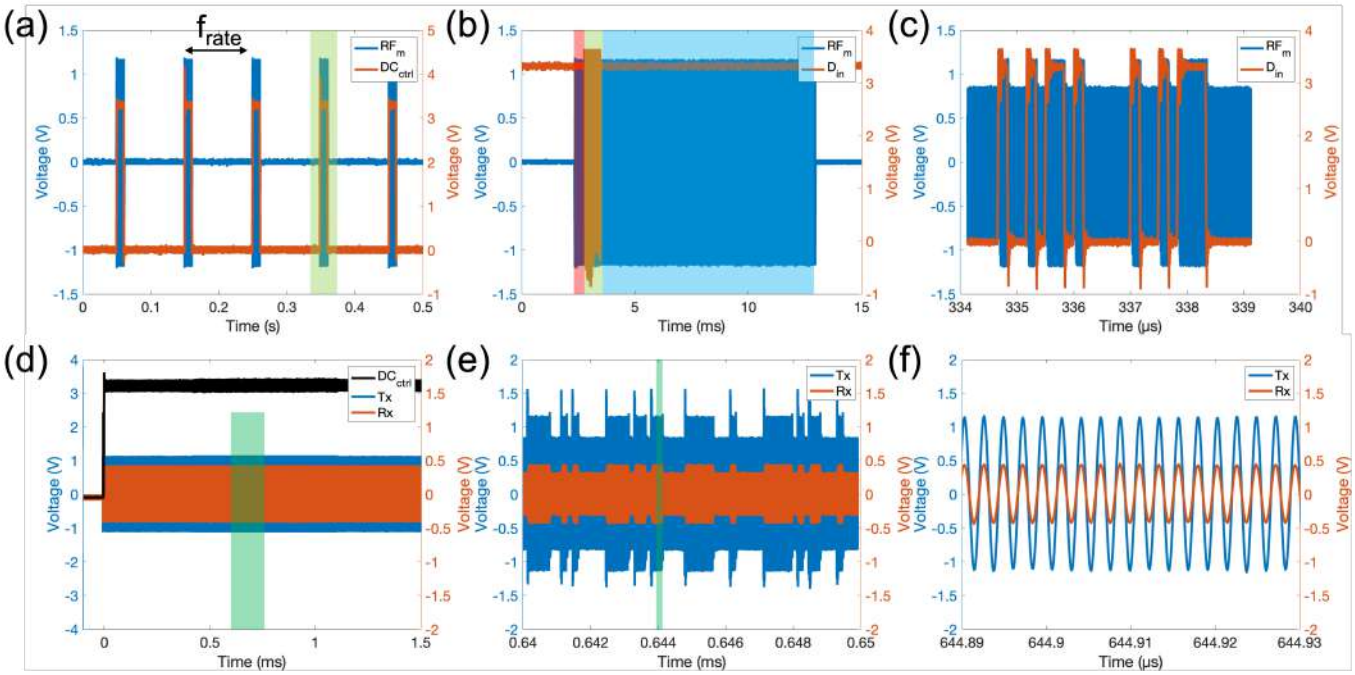

Figure 9. (a) Real-time measurement of a 0.5 s duty cycled power and data transmission RF_m (blue) with f_{rate} = 10 Hz triggered by DC_{ctrl} (orange) at DC = 10%. (b) Single frame time-locked division: power-on preamble (red), addressing time (green) and stimulating time (light blue). (c) Magnification of the transmitted RF_m signal (blue) ASK-modulated by D_{in} (orange) at 6 Mbps highlighting two 14-bits strings. (d) Real-time ex-vivo IPT transmission highlighting the Tx carrier (blue) and the Rx received signal (orange) triggered by DC_{ctrl} (black). (e) Green-strip magnification including power and data transmission at f_{data} = 6 Mbps respectively at Tx (blue) and Rx (orange) levels. (f) Magnification of the sinusoidal transmitted (blue) and received (orange) signals at 433.92 MHz.

safely delivering a maximum of 11 mW to each miniaturised Rx distributed below the Res area. This power is enough for intracortical microstimulation to evoke phosphenes in the human visual cortex [34].

D. Entire system

Figure 8 shows the testing setup of the entire real-time system where relevant testing signals are extracted from the device (i.e., DC_{ctrl} and D_{in}) and the output powering carrier RF_m is attenuated by 20 dB. Figure 9(a) shows a 0.5 s real-time duty cycled power and data transmission (RF_m, blue) with f_{rate} = 10 Hz triggered by DC_{ctrl} (orange) with a duty cycle of 10%. The green strip region of a single frame is magnified in Figure 9(b) highlighting the timely-locked division already presented in Figure 2(a). In particular, the power-on preamble time is in red, the addressing time in green and the stimulating time in light blue. Two consecutive 14-bits strings are highlighted in Figure 9(c) where the powering carrier RF_m (blue) is ASK-modulated by the high-speed data D_{in} (orange) for a data rate f_{data} = 6 Mbps. A stable negligible delay of 50 ns is observed between the digitalisation and the analog modulation. The entire transmission system is measured by combining the real-time experimental setup of Figure 8 together with the 3-coil IPT setup of Figure 7(a). Figure 9(d),(e) respectively show the entire and magnified (green strip) real-time ex-vivo IPT transmission triggered by DC_{ctrl} (black) and highlighting the Tx carrier (blue) and the Rx received signal (orange). Figure 9(f) shows the transmitted (blue) and received (orange) sinusoidal signal at 433.92 MHz, highlighting no morphological distortion on the Rx waveform due to the IPT link. The system permits the wireless power transmission of 32 dBm potentially allowing the simultaneous communication with 1024 miniaturised receivers at a maximum data rate of 6 Mbps. Despite the integrated receiver is not implemented and demonstrated in this paper, the transmitter performances are adapted to work with state-of-the-art integrated demodulators. A clock and data recovering circuit has been recently reported with standard 180-nm CMOS technology to allow the reconstruction of the transmitted digital data D_{in} at 6 Mbps in a silicon area of 17×89 μm^2 [42].

The wearable system is 181×84.5×32.5 mm^3 and weighs 832 g including all the components in a plastic case (Figure 10(a)) except the camera and the Tx. Figure 10(b) shows the real functional blocks of the fabricated WTU including PMU (orange), MCU (green), PO (blue), PLL (purple), ASK (grey) and PA (red) circuits.

The system consumes a total of 9100 mW, including the image acquisition and the VPU in the RPi. Figure 10(c) shows the power contribution of the VPU and the WTU, including the PO, the ASK, the PLL and the PA. In particular, the class-AB PA overall consumes 3412 mW for the high wireless power transmission of 1584 mW (32 dBm). The real-time VPU accounts itself for half of the power consumption

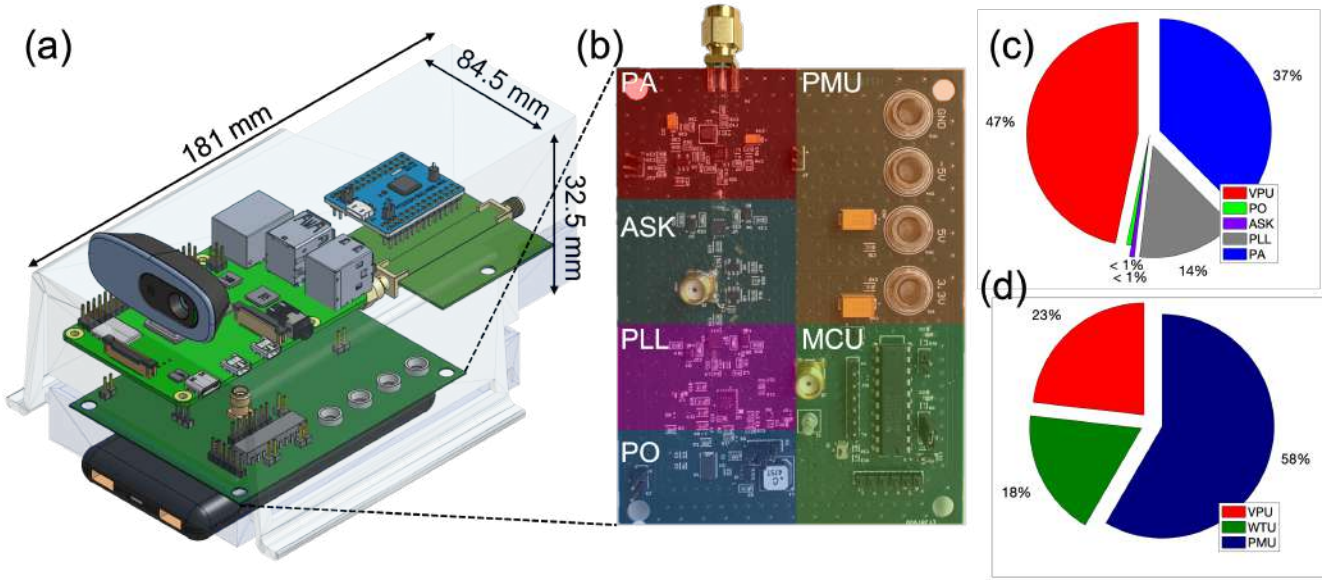

Figure 10. (a) Render assembling of the wearable real-time SWIPT system. (b) Image of the fabricated WTU including PMU (orange), MCU (green), PO (blue), PLL (purple), ASK (grey) and PA (red) circuits. (c) Total power consumption of the system (9100 mW) distributed among VPU and WTU including PO, ASK, PLL and PA for a total transmitted power of 32 dBm. (d) Weight distribution (832 g) among VPU, WTU and PMU.

(47%), due to the computationally intensive nature of image processing algorithms in general. This comes from a RPi-based VPU, which allows an easier, flexible and versatile approach. Figure 10(d) shows the weight contribution for the different units. The rechargeable battery is the heaviest element (i.e., 486 g). The latter has a capacity of 82.8 Wh and the capability to continuously supply the entire system for 9 hours. Envisioning an in-vivo validation, non-human primates such as monkeys are usually capable to run 1000-3000 trials of behavioral and stimulation tasks in a 2-3 hours' timeframe during each experimental session [34], [43]. Therefore, the developed system is suitable for conducting pre-clinical in-vivo validations toward the development of a wireless and distributed CVP [34].

Table II compares the proposed wearable system with the state-of-the-art, highlighting the key parameters for wireless power and data transmission to CVP. As expected, OOK and ASK provide the highest data rate [23], [37], [40]. On the other hand, in miniaturised chips, OOK modulation is critical in providing a stable supply at the implant side, as no power is transmitted for the low logical state. In one work, the data rate is 20 Mbps, exploiting Phase-Shift Keying (PSK) modulation while not operating as a SWIPT system [21]. In particular, two different wireless channels are used respectively for power and data communication. This approach is not possible with miniaturised and distributed neural implants as it would require two antennas at the receiving side. The proposed real-time and wearable SWIPT system provides the highest output power of 32 dBm and exploits the ASK modulation technique for achieving maximum data rates of 6 Mbps and 20 Mbps respectively considering the full system and the WTU only. FOM_1 [31] summarises the performances of the systems considering the maximum data rate and the carrier frequency. However, the system capability of transmitting enough power is fundamental in the case of miniaturised neural implants. Therefore, FOM_2 also considers the maximum output power and the system efficiency η_S. It is worth to notice that that not all the works rely on SWIPT system [21], [19], thus, the output power and/or the η_S are not always mentioned in their results. Also, most of the SWIPT systems of Table II use a class-E PA, which usually ensures efficiencies higher than 90%. Although the chosen class-AB PA lacks in efficiency (i.e., high power consumption for a fixed output power with respect to a class-E PA [23]), class-AB PA represents a trade-off between high output power, high carrier frequency, linearity, efficiency, and robustness in terms of susceptibility to the network load, as already shown in [31], [40]. Additionally, this work presents the maximum obtainable performances considering the external SWIPT system without any integrated demodulator at Rx side, similarly to [39]. Instead, it is fair mentioning that some works considered the overall performances of the transceiver for their time-lagged [36], [37] or real-time operations [20], [41]. Then, differently from [19] and [20], the proposed real-time RPi-based system integrates both hardware and software in the same wearable device. However, future implementations might envision the use of FPGA toward an optimised VPU from a power consumption viewpoint. It is also worth noting that most of the previous work targeting visual prosthesis [19], [20], [41] operate with lower carrier frequencies in the range of 10-20 MHz [20], [41]. This is preferred when powering relatively large implants (i.e., tens of millimeters to centimeter ranges) to limit tissue adsorption. However, as previously mentioned, with multiple miniaturised receivers freely distributed, the operating frequency must increase toward several hundreds of MHz [32], thus, being the realised system usable with the next-generation of wireless and distributed BMI.

Table II: STATE-OF-THE-ART COMPARISON OF WIRELESS POWER AND DATA TRANSMITTERS.

Type, Ref.	Freq. (MHz)	Mod. Tech.	Data Rate (Mbps)	Power (dBm)	η_S (%)	Demod.	SWIPT	Real Time	Wearable	FoM$_1^a$	FoM$_2^b$
G, [35]	0.7	ASK	0.06	17	36	Yes$^{\triangle}$	Yes	No	No	0.17	3.11
G, [36]	13.56	PDM	13.56**	25.3	61.8	Yes	Yes	No	H[1]	2.38	499
G, [23]	10	ASK	1	13.8	42	Yes$^{\triangle}$	Yes	No	No	0.46	4.67
C, [37]	1000	PWM-ASK	1	8	NA	Yes	Yes	No	No	0.10	NA
G, [38]	13.56	BPSK	3.39	14.9	NA	Yes	Yes	No	No	0.95	N/A
G, [39]	1	SCM	0.5	15.1	61	No	Yes	No	No	0.63	12.4
G, [40]	2400	OOK	4	3	34.1	Yes	Yes	No	H[1]	0.19	0.12
IO, [21]	10**	PSK	20**	NA	NA	Yes	No	No	No	3.42	NA
E, [19]	20	DPSK	2	NA	NA	Yes	No	Yes*	No	0.58	NA
C, [20]	10	FSK	1	17	NA	Yes	Yes	Yes*	H[1]	0.46	NA
C, [41]	13.56	OOK	1.5	NA	NA	Yes	Yes	Yes*	H/S[1]	0.54	NA
IC, This work	**433**	**DC-ASK**	**6/20$^{\#}$**	**32**	**17.4/32.6$^{\#}$**	**No**	**Yes**	**Yes$^{\bullet}$**	**H/S[1]**	**0.43/0.97$^{\#}$**	**120/503$^{\#}$**

G: General; IO: Intraocular; E: Epiretinal; C: Cortical; IC: Intracortical. [a] $FOM_1 = \left(\frac{Datarate^2}{f_c}\right)^{1/3}$.
[b] $FOM_2 = \left(\frac{Datarate^2}{f_c}\right)^{1/3} \cdot Power \cdot \frac{\eta_S}{100}$. #WTU Only. *FPGA. •RPi. **Different channels for power and data.
[1]H: Hardware; S: Software. $^{\triangle}$Off-the-shelf.

IV. Conclusion

In this work, a wearable real-time system has been designed, developed, and validated both in air and in ex-vivo. The main key parameters, such as real-time frame rate, single-band powering frequency, communication data rate, output power, and specific adsorption rate were combined to develop a simultaneous wireless information and power transfer system. The latter included in a single wearable device a software-based visual processing unit for real-time image capturing, processing, and data generation; a hardware transmitting unit coupled with amplitude shift keying modulation; and a high-frequency 3-coil inductive link ensuring safe wireless power transfer and potentially allowing simultaneous communication with 1024 miniaturised and distributed intracortical microstimulators. Results enable the utilization of wireless, miniaturised and distributed neural interfaces in the development of the upcoming generation of wireless and large-scale cortical visual prosthesis.

V. Acknowledgement

This work was supported by the Interdisciplinary Seed Fund from École Polytechnique Fédérale de Lausanne. The Authors would like to thank Mr. Ali Meimandi, Mrs. Barbara Gentile, Mr. Edouard Koehn, Mr. Simone Emiliani, Mrs. Desirée Maulà and Mr. Alexandre Lechartier for their help.

References

[1] S. Saha et al. "Progress in brain computer interface: Challenges and opportunities". In: *Frontiers in systems neuroscience* 15 (2021), p. 578875.
[2] A. Nurmikko. "Challenges for large-scale cortical interfaces". In: *Neuron* 108.2 (2020), pp. 259–269.
[3] K. M. Szostak et al. "Distributed Neural Interfaces: Challenges and Trends in Scaling Implantable Technology". In: *Handbook of Neuroengineering* (2021), pp. 1–37.
[4] G. L. Barbruni et al. "Miniaturised wireless power transfer systems for neurostimulation: A review". In: *IEEE Transactions on Biomedical Circuits and Systems* 14.6 (2020), pp. 1160–1178.
[5] M. M. Ghanbari et al. "A sub-mm 3 ultrasonic free-floating implant for multi-mote neural recording". In: *IEEE Journal of Solid-State Circuits* 54.11 (2019), pp. 3017–3030.

[6] J. Lee et al. "Neural recording and stimulation using wireless networks of microimplants". In: *Nature Electronics* 4.8 (2021), pp. 604–614.

[7] A.-H. Lee et al. "A scalable and low stress post-CMOS processing technique for implantable microsensors". In: *Micromachines* 11.10 (2020), p. 925.

[8] P. Yeon et al. "Microfabrication, coil characterization, and hermetic packaging of millimeter-sized free-floating neural probes". In: *IEEE Sensors Journal* 21.12 (2021), pp. 13837–13848.

[9] N. Ahmadi et al. "Towards a distributed, chronically-implantable neural interface". In: *2019 9th International IEEE/EMBS Conference on Neural Engineering (NER)*. IEEE. 2019, pp. 719–724.

[10] D. Ghezzi. "The role of the visual field size in artificial vision". In: *Journal of Neural Engineering* 20.2 (2023), p. 023001.

[11] G. S. Brindley and W. S. Lewin. "The sensations produced by electrical stimulation of the visual cortex". In: *The Journal of physiology* 196.2 (1968), pp. 479–493.

[12] W. H. Dobelle, M. G. Mladejovsky, and J. P. Girvin. "Artificial vision for the blind: electrical stimulation of visual cortex offers hope for a functional prosthesis". In: *Science* 183.4123 (1974), pp. 440–444.

[13] P. R. Troyk. "The intracortical visual prosthesis project". In: *Artificial vision: a clinical guide* (2017), pp. 203–214.

[14] J. V. Rosenfeld et al. "Tissue response to a chronically implantable wireless intracortical visual prosthesis (Gennaris array)". In: *Journal of neural engineering* 17.4 (2020), p. 046001.

[15] D. Tsai et al. "A wearable real-time image processor for a vision prosthesis". In: *Computer methods and programs in biomedicine* 95.3 (2009), pp. 258–269.

[16] W. H. Li. "A fast and flexible computer vision system for implanted visual prostheses". In: *Computer Vision-ECCV 2014 Workshops: Zurich, Switzerland, September 6-7 and 12, 2014, Proceedings, Part III 13*. Springer. 2015, pp. 686–701.

[17] B. Lee and M. Ghovanloo. "An overview of data telemetry in inductively powered implantable biomedical devices". In: *IEEE Communications Magazine* 57.2 (2019), pp. 74–80.

[18] S. A. Mirbozorgi et al. "A single-chip full-duplex high speed transceiver for multi-site stimulating and recording neural implants". In: *IEEE transactions on biomedical circuits and systems* 10.3 (2015), pp. 643–653.

[19] Y.-K. Lo et al. "A Fully-Integrated High-Compliance Voltage SoC for Epi-Retinal and Neural Prostheses". In: *IEEE Transactions on Biomedical Circuits and Systems* 7.6 (2013), pp. 761–772.

[20] M. Piedade et al. "Visual neuroprosthesis: a non invasive system for stimulating the cortex". In: *IEEE Transactions on Circuits and Systems I: Regular Papers* 52.12 (2005), pp. 2648–2662.

[21] M. Monge et al. "A fully intraocular high-density self-calibrating epiretinal prosthesis". In: *IEEE transactions on biomedical circuits and systems* 7.6 (2013), pp. 747–760.

[22] M. K. Raja and Y. P. Xu. "A 52 pJ/bit OOK Transmitter with adaptable data rate". In: *2008 IEEE Asian Solid-State Circuits Conference*. IEEE. 2008, pp. 341–344.

[23] M.L. Navaii, H. Sadjedi, and A. Sarrafzadeh. "Efficient ASK data and power transmission by the class-E with a switchable tuned network". In: *IEEE Transactions on Circuits and Systems I: Regular Papers* 65.10 (2018), pp. 3255–3266.

[24] G. L. Barbruni, D. Ghezzi, and S. Carrara. "Challenges for Miniaturized Neurostimulators: Design of wireless Bio/CMOS interfaces for brain stimulation". In: *IEEE Solid-State Circuits Magazine* 15.2 (2023), pp. 34–40.

[25] M. Kiani, U.-M. Jow, and M. Ghovanloo. "Design and optimization of a 3-coil inductive link for efficient wireless power transmission". In: *IEEE transactions on biomedical circuits and systems* 5.6 (2011), pp. 579–591.

[26] R. Hartley. "RF/Microwave PC Board Design and Layout". In: *L-3 Avionics Systems* (2005).

[27] A. J. Burkhardt, C. S. Gregg, and J. A. Staniforth. "Calculation of PCB track impedance". In: *Circuit World* 26.1 (2000), pp. 6–10.

[28] D. Ahn and M. Ghovanloo. "Optimal design of wireless power transmission links for millimeter-sized biomedical implants". In: *IEEE transactions on biomedical circuits and systems* 10.1 (2015), pp. 125–137.

[29] P. Feng et al. "Chip-scale coils for millimeter-sized bio-implants". In: *IEEE transactions on biomedical circuits and systems* 12.5 (2018), pp. 1088–1099.

[30] A. Khalifa et al. "The microbead: A 0.009 mm 3 implantable wireless neural stimulator". In: *IEEE transactions on biomedical circuits and systems* 13.5 (2019), pp. 971–985.

[31] G. L. Barbruni et al. "A 20 Mbps, 433 MHz RF ASK transmitter to inductively power a distributed network of miniaturised neural implants". In: *2021 IEEE International Symposium on Medical Measurements and Applications (MeMeA)*. IEEE. 2021, pp. 1–6.

[32] A. S.Y. Poon, S. O'Driscoll, and T. H. Meng. "Optimal frequency for wireless power transmission into dispersive tissue". In: *IEEE Transactions on Antennas and Propagation* 58.5 (2010), pp. 1739–1750.

[33] S. A. Mirbozorgi, P. Yeon, and M. Ghovanloo. "Robust wireless power transmission to mm-sized free-floating distributed implants". In: *IEEE transactions on biomedical circuits and systems* 11.3 (2017), pp. 692–702.

[34] E. Fernández et al. "Visual percepts evoked with an intracortical 96-channel microelectrode array inserted in human occipital cortex". In: *The Journal of clinical investigation* 131.23 (2021).

[35] M. Catrysse, B. Hermans, and R. Puers. "An inductive power system with integrated bi-directional data-transmission". In: *Sensors and Actuators A: Physical* 115.2-3 (2004), pp. 221–229.

[36] M. Kiani and M. Ghovanloo. "A 13.56-Mbps pulse delay modulation based transceiver for simultaneous near-field data and power transmission". In: *IEEE transactions on biomedical circuits and systems* 9.1 (2014), pp. 1–11.

[37] J. Lee et al. "Wireless Ensembles of Sub-mm Microimplants Communicating as a Network near 1 GHz in a Neural Application". In: *bioRxiv* (2020).

[38] M. Chen et al. "A 70%-power transmission efficiency, 3.39 Mbps power and data telemetry over a single 13.56 MHz inductive link for biomedical implants". In: *Science China Information Sciences* 66.2 (2023), p. 122406.

[39] K. Dehghan, O. Shoaei, and S. J. Ashtiani. "A Class-E Power and Data Transmitter With Improved Data Rate to Carrier Frequency Ratio for Medical Implants". In: *IEEE Transactions on Circuits and Systems II: Express Briefs* 69.6 (2022), pp. 2692–2696.

[40] Q. Zhang, X. Kuang, and N. Wu. "An ultra-low-power RF transceiver for WBANs in medical applications". In: *Journal of Semiconductors* 32.6 (2011), p. 065008.

[41] J. Coulombe, M. Sawan, and J.-F. Gervais. "A highly flexible system for microstimulation of the visual cortex: Design and implementation". In: *IEEE transactions on biomedical circuits and systems* 1.4 (2007), pp. 258–269.

[42] M. Cerbai et al. "An Ultra-Miniaturised CMOS Clock and Data Recovery System for Wireless ASK Transmission". In: *2023 IEEE International Symposium on Circuits and Systems (ISCAS)* (2023), pp. 1–5.

[43] P. H. Schiller et al. "New methods devised specify the size and color of the spots monkeys see when striate cortex (area V1) is electrically stimulated". In: *Proceedings of the National Academy of Sciences* 108.43 (2011), pp. 17809–17814.

Gian Luca Barbruni was born in Sanremo (IM), Italy in 1995. He received both the B.Sc. and M.Sc. degrees in Biomedical Engineering from the Politecnico di Torino, Turin, Italy in 2017 and 2019 respectively. He was a Research Associate at the Department of Electronic Engineering (DET) and MiNES (Micro&Nano Electronic Systems) Laboratory at Politecnico di Torino. Actually he is conducting his Ph.D. in Microsystems and Microelectronics (EDMI) at École Polytechnique Fédérale de Lausanne - Microcity, Neuchâtel, Switzerland. His project is focused on the development of miniaturised neuroprosthesis device for artificial vision. His current research interests include neural prosthesis, biosensors, wireless power transfer and data communication, ultra-low-power and miniaturised CMOS integrated circuits for the development of innovative biomedical systems.

Francesca Rodino received the B.Sc. and M.Sc. degrees in Biomedical Engineering from the Politecnico di Torino, Turin, Italy, in 2019 and 2022, respectively. She developed her Master's project in the field of cortical neuroprosthesis devices for artificial vision in collaboration with the Integrated Circuits Laboratory (ICLAB) at École Polytechnique Fédérale de Lausanne (EPFL) in Neuchâtel. Currently, she is conducting her Ph.D. in Microsystems and Microelectronics (EDMI) at EPFL's Electrical and Microengineering Institute (IEM) - Microcity, Neuchâtel, Switzerland. Her Ph.D. project is focused on developing an intelligent platform for drug response in precision oncology. Her current research interests include electrochemical biosensors and frontend electronics for multiple drug monitoring in personalized medicine and therapy.

Paolo Motto Ros (M'16) received the M.Sc. and Ph.D. degrees in electronic engineering from the Politecnico di Torino, Italy, in 2005 and 2009, respectively. Assistant Professor at Politecnico di Torino, Department of Electronics and Telecommunications, Turin, Italy. Post-doc researcher at Politecnico di Torino (2009-2012), senior (since 2014) post-doc researcher at Istituto Italiano di Tecnologia (2012-2019), senior post-doc researcher and adjunct professor (since 2017) at Politecnico di Torino (2019-2022). Author and co-author of more than 80 international scientific publications. Dr. Motto Ros was member of the organizing committee of IEEE ICECS 2019, the FoodCAS Satellite Event at IEEE ISCAS 2021, and IEEE CAFE 2023; review committee member of IEEE BioCAS 2021–2023, special session organizer at IEEE MeMeA 2021, program committee member of IEEE LASCAS 2022 and 2023, guest editor of MDPI Sensors and guest associate editor of Frontiers in Neurorobotics. He is Associate Editor of IEEE Transactions on Biomedical Circuits and Systems and IEEE Transactions on AgriFood Electronics.

Danilo Demarchi (M'10-SM'13) received Engineering Degree and Ph.D. in electronics engineering from Politecnico di Torino, Italy, in 1991 and 1995, respectively. Full Professor at Politecnico di Torino, Department of Electronics and Telecommunications, Turin, Italy. Visiting Professor at Tel Aviv University (2018-2021) and at EPFL Lausanne (2019). Visiting Scientist at MIT and Harvard Medical School (2018). Author and co-author of 5 patents and more than 350 international scientific publications. Prof. Demarchi is the leader of the eLiONS (electronic LIfe-Oriented iNtelligent Systems) Laboratory at Politecnico di Torino. Founder and Editor in Chief of the IEEE Transactions on AgriFood Electronics (TAFE). Founder and General-Co-Chair of the IEEE Conference on AgriFood Electronics (CAFE). Founder and Vice-Chair of the IEEE CAS Special Interest Group on AgriFood Electronics. 2023-2024 Distinguished Lecturer for the IEEE CAS Society with the Lecture "Let the Plants Do the Talking: Smart Agriculture by the messages received from Plants and Soil". Member of the IEEE Sensors Council and the BioCAS Technical Committee. Associate Editor of the IEEE Open Journal on Engineering in Medicine and Biology (OJ-EMB) and the Springer-Nature Journal BioNanoScience. Senior Member of IEEE. General Chair of IEEE BioCAS Conference in 2017 in Torino and founder of the IEEE FoodCAS Workshop (Circuits and Systems for the FoodChain). TPC Co-Chair of IEEE ICECS 2019, IEEE BioCAS 2021 and IEEE BioCAS 2022 conferences. General Co-Chair of IEEE BioCAS 2023. Organizer of the 3rd Seasonal School on AgriFood Electronics: Smart Technologies for a Sustainable Agriculture in Torino, September 2022.

Diego Ghezzi received his M.Sc. in Biomedical Engineering (2004) and Ph.D. in Bioengineering (2008) from Politecnico di Milano. From 2008 to 2013, he completed his postdoctoral training at Istituto Italiano di Tecnologia in Genova at the Department of Neuroscience and Brain Technologies, where he was promoted to Researcher in 2013. In 2015, he was appointed Assistant Professor of Bioengineering with the Medtronic Chair in Neuroengineering at the Center for Neuroprosthetics and Institute of Bioengineering of the École Polytechnique Fédérale de Lausanne. Since 2023, he is direct of Surgical technologies and innovations at the Hôpital ophtalmique Jules-Gonin in Lausanne. His laboratory, the Ophthalmic and Neural Technologies laboratory, is a multidisciplinary environment promoting cross-fertilization among diverse expertise. It brings materials science, engineering, computer science, life science, and medicine together by the convergence of physicists, engineers, neuroscientists, and ophthalmologists cooperating to accomplish innovative projects. The mission is to develop innovative ophthalmic and neural technologies to better understand diseases and, eventually, improve the quality of life of people with ophthalmic and neural disorders. Ultimately, we aim at translating our research findings into clinical practice.

Sandro Carrara (F'15) is an IEEE Fellow and also the recipient of the IEEE Sensors Council Technical Achievement Award. He is a professor and head of the Bio/CMOS Interfaces Laboratory at the EPFL in Lausanne (CH). He is a former professor at the Universities of Genoa and Bologna (IT). He holds a Ph.D. in Biochemistry and Biophysics from the University of Padua (IT), a Master degree in Physics from the University of Genoa (IT), and a diploma in Electronics from the National Institute of Technology in Albenga (IT). Along his carrier, he published 7 books with prestigious publishers such as Springer/NATURE and Cambridge University Press. He has more than 380 scientific publications and is author of 17 patents. He is Editor-in-Chief of the IEEE Sensors Journal, one of the largest journals among 220 IEEE publications, and Associate Editor of the IEEE Transactions on Biomedical Circuits and Systems. He is a member of the IEEE Sensors Council and its Executive Committee. He was in the Board of Governors (BoG) of the IEEE CAS Society.